

High-Frequency EPR and ENDOR Spectroscopy of Mn^{2+} Ions in CdSe/CdMnS Nanoplatelets

Roman A. Babunts,* Yulia A. Uspenskaya, Nikolai G. Romanov, Sergei B. Orlinskii, Georgy V. Mamin, Elena V. Shornikova,* Dmitri R. Yakovlev,* Manfred Bayer, Furkan Isik, Sushant Shendre, Savas Delikanli, Hilmi Volkan Demir, and Pavel G. Baranov



Cite This: *ACS Nano* 2023, 17, 4474–4482



Read Online

ACCESS |

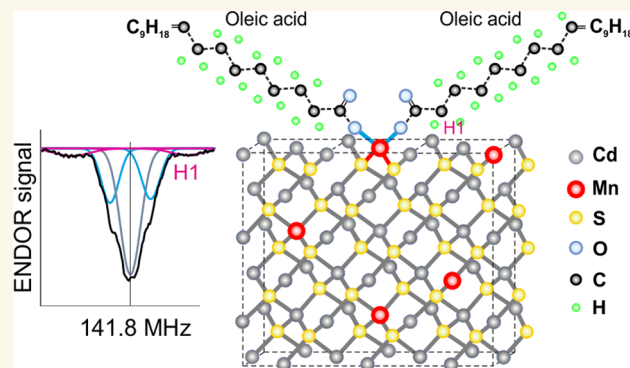
Metrics & More

Article Recommendations

Supporting Information

ABSTRACT: Semiconductor colloidal nanoplatelets based of CdSe have excellent optical properties. Their magneto-optical and spin-dependent properties can be greatly modified by implementing magnetic Mn^{2+} ions, using concepts well established for diluted magnetic semiconductors. A variety of magnetic resonance techniques based on high-frequency (94 GHz) electron paramagnetic resonance in continuous wave and pulsed mode were used to get detailed information on the spin structure and spin dynamics of Mn^{2+} ions in core/shell CdSe/(Cd,Mn)S nanoplatelets. We observed two sets of resonances assigned to the Mn^{2+} ions inside the shell and at the nanoplatelet surface. The surface Mn demonstrates a considerably longer spin dynamics than the inner Mn due to lower amount of surrounding Mn^{2+} ions. The interaction between surface Mn^{2+} ions and ^1H nuclei belonging to oleic acid ligands is measured by means of electron nuclear double resonance. This allowed us to estimate the distances between the Mn^{2+} ions and ^1H nuclei, which equal to 0.31 ± 0.04 , 0.44 ± 0.09 , and more than 0.53 nm. This study shows that the Mn^{2+} ions can serve as atomic-size probes for studying the ligand attachment to the nanoplatelet surface.

KEYWORDS: colloidal nanocrystals, CdSe nanoplatelets, diluted magnetic semiconductors, electron paramagnetic resonance, electron nuclear double resonance



Colloidal nanoplatelets (NPLs) based on II–VI semiconductors are two-dimensional nanocrystals, which are flat at the atomic level and have several monolayer thickness.^{1–6} Their surface is passivated by organic ligands, which are covalently bound to it. These ligands ensure chemical integrity of the nanocrystals and colloidal stability. The optical and spin properties of bare core nanocrystals are greatly determined by the surface properties.^{7–9} The core can be overgrown by a semiconductor shell with a wider bandgap than the core material, which reduces the surface influence on the charge carriers and excitons confined in the core. It was shown that in core/shell NPLs, the quantum yield and structural stability under light illumination are significantly increased.^{10,11}

The spin properties and magneto-optical effects in diluted magnetic semiconductors (DMS) are greatly modified by doping with magnetic impurities.¹² Band-offset engineering and tunable magnetic exchange interactions were demonstrated in various magnetic/nonmagnetic semiconductor nanostruc-

tures, including colloidal quantum dots and NPLs.^{13–17} Manganese is considered as an extremely informative magnetic impurity for electron paramagnetic resonance (EPR), since any of its charge states has paramagnetic properties. For Mn^{2+} ions, which are characterized by a half-filled $3d^5$ electron shell, the orbital angular momentum vanishes, that is, the S -state $^6S_{5/2}$ is realized. A distinctive feature of such ions is the ability to provide EPR spectra in a wide range of temperatures, including cryogenic and above room temperatures, due to long spin–lattice relaxation times.

Received: October 11, 2022

Accepted: February 15, 2023

Published: February 20, 2023



In colloidal synthesis, the exact location and concentration of Mn^{2+} ions cannot be controlled with high accuracy, such as in molecular-beam epitaxy. Therefore, techniques providing this information for grown nanocrystals are important, among them magnetic resonance techniques are well suited for that. EPR was used to study manganese-doped II–VI colloidal nanocrystals; see refs 18–26 and references therein. It was shown that Mn^{2+} ions that substitute metal ions inside the semiconductor core of nanocrystals and at their surface differ significantly in their hyperfine structure. Mn-doped colloidal nanocrystals were mainly studied by EPR in continuous wave mode. Although pulsed EPR gives access to the spin relaxation dynamics and electron nuclear double resonance (ENDOR) provides information on the Mn surrounding, reports on such measurements in colloidal nanocrystals are rare.^{22–26} Optical and magneto-optical investigations of Mn-doped NPLs were carried out,^{15,16,18,27} including optically detected magnetic resonance (ODMR).^{27–29} However, no detailed EPR studies of DMS NPLs were reported.

In this paper, we study core/shell CdSe/(Cd,Mn)S NPLs with 1% and 4% Mn concentration using several magnetic resonance techniques: (i) high-frequency (W-band, 94 GHz) EPR operating in continuous wave (CW) and pulsed (electron spin echo, ESE) mode in a temperature range from 1.6 to 30 K, and (ii) high-frequency ESE-detected ENDOR of Mn^{2+} ions. We show that Mn^{2+} ions occupy cation positions both inside the NPL shell and at the NPL surface, acting as individual ions or complexes of interacting ions. Spin parameters and spin dynamics of these Mn^{2+} ions depend strongly on their location. We observe interaction of surface Mn^{2+} ions and hydrogen inside the oleic acid ligands attached to this ion by ENDOR.

RESULTS AND DISCUSSION

Two samples of core/shell NPLs with CdSe/(Cd,Mn)S (sample #1) and CdSe/(Cd,Zn,Mn)S (sample #2) composition were used for this study. Details of their synthesis are given in the Supporting Information S1 and can be found also in refs 6, 15, and 30. The samples have 2-monolayer-thick CdSe cores and 5-monolayer-thick shells cladding the core. NPLs have totally 12 halogen and 13 metal layers, so that the top and bottom facets are terminated with Cd(Mn). The Mn concentration in the shells is 1% in the sample #1 and 4% in the sample #2. The Mn concentrations were estimated by measuring the spin–lattice relaxation times (see refs 27 and 29 for the method description). In the sample #2, a small concentration of zinc (about 8%) was added to the (Cd,Zn,Mn)S shell. The NPL parameters are listed in Table 1. Information on the optical and magneto-optical properties of similar samples can be found in refs 15, 27, and 29. It is important to note that the evaluation of the Mn concentration incorporated in the layers of colloiddally grown nanoplatelets is rather nontrivial. Commonly the inductively coupled plasma mass spectrometry (ICP-MS) is used for that to

analyze the solution with the nanoplatelets. These results should be taken as a rough evaluation. We have developed recently a magneto-optical technique, which uses an exciton as an internal probe within the CdSe core of CdSe/(Cd,Mn)S NPLs. It allows us by means of the giant Zeeman effect to measure the exciton exchange interaction with the Mn spins and the spin–lattice relaxation dynamics of the Mn spin system. The Mn spin–lattice relaxation time is strongly sensitive to the Mn concentration, as the relaxation process goes via Mn–Mn interactions. As a result, the Mn concentration can be evaluated with high accuracy. We have shown in ref 27 that there is a considerable misfit in the data received by the magneto-optical and ICP-MS techniques in CdSe/(Cd,Mn)S NPLs. This difference also takes place for the samples studied in the present paper; see Table 1. A possible reason for that could be that the ICP-MS technique measures the integral characteristic of the NPL ensembles in solution, where also uncleaned unreacted products may contribute.

CW and ESE-Detected EPR. Figure 1a shows the CW EPR spectra recorded at a frequency of 94 GHz on CdSe/(Cd,Mn)S NPLs, sample #1, in the temperature range of 1.6–20 K. The EPR spectra at temperatures above 3 K consist of two well-resolved sextets of lines corresponding to Mn^{2+} ions with two different hyperfine structure constants $A = 7.0$ mT and 9.3 mT. We attribute the EPR spectra with smaller A to Mn^{2+} replacing cadmium inside the (Cd,Mn)S shell, since this value is close to the 6.9 mT known for bulk (Cd,Mn)S,³¹ and will call these Mn^{2+} ions “inner Mn”. Note that the hyperfine structure constant of Mn^{2+} ions in solids strongly depends on the degree of the material covalence. In semiconductors, it increases for decreasing degree of covalence, while it reaches its maximum value in materials with a strong ionic bond, in particular, in dielectric fluorite crystals.³² The reason for these changes is discussed in the Supporting Information S3. We attribute the EPR spectra with the larger A to Mn^{2+} ions at the NPL surface and designate them as “surface Mn”. The surface Mn has two electrons, which interact with the oxygen of the oleic acid. Oxygen bonds usually lead to a weakening of covalence and, therefore, result in larger A .

At lower temperatures (1.6–3 K), the intensity of the resolved Mn^{2+} spectra decreases and an intense broad line appears (Figure 1a). It has a shape close to Lorentzian with the width ΔB about 60 mT at 1.6 K. Figure 1b displays the ESE-detected EPR spectra measured in the same sample at 1.6 to 3 K. The $\pi/2 - \tau - \pi$ microwave pulse sequence (Hahn echo sequence) was used with the $\pi/2$ pulse length of 100 ns and the delay τ between the $\pi/2$ and π pulses $\tau = 500$ ns (the π pulse is twice longer than the $\pi/2$ pulse). For comparison, the CW EPR spectrum measured at 3 K is also shown. In the ESE-detected EPR spectra, the intense Lorentzian-shape broad line is similar to the line observed in the low-temperature CW EPR spectra in Figure 1a. The large amplitude of this contour is apparently a manifestation of superparamagnetic properties arising at low temperatures from the interaction between Mn^{2+} ions, most likely surface Mn.

In Figure 1c the CW EPR spectrum measured at $T = 5$ K is shown (upper spectrum, black line). It is a superposition of signals coming from the inner and surface Mn, which contributions can be separated and measured individually from the two outputs, “sin” (blue line) and “cos” (red line), of the in-phase and quadrature-phase (IQ) detector of the microwave bridge (Methods). This is possible because the two types of Mn ions have different spin relaxation times. Schematically, the locations of the inner and surface Mn ions are indicated in Figure 1d.

Table 1. NPL Parameters

Sample	Composition of core/shell NPLs	Number of core/shell monolayers	Mn concentration estimated from ICP-MS (%)	Mn concentration estimated from Mn spin–lattice relaxation time (%)
#1	CdSe/(Cd,Mn)S	2/5	3	1
#2	CdSe/(Cd,Zn,Mn)S	2/5	1.6	4

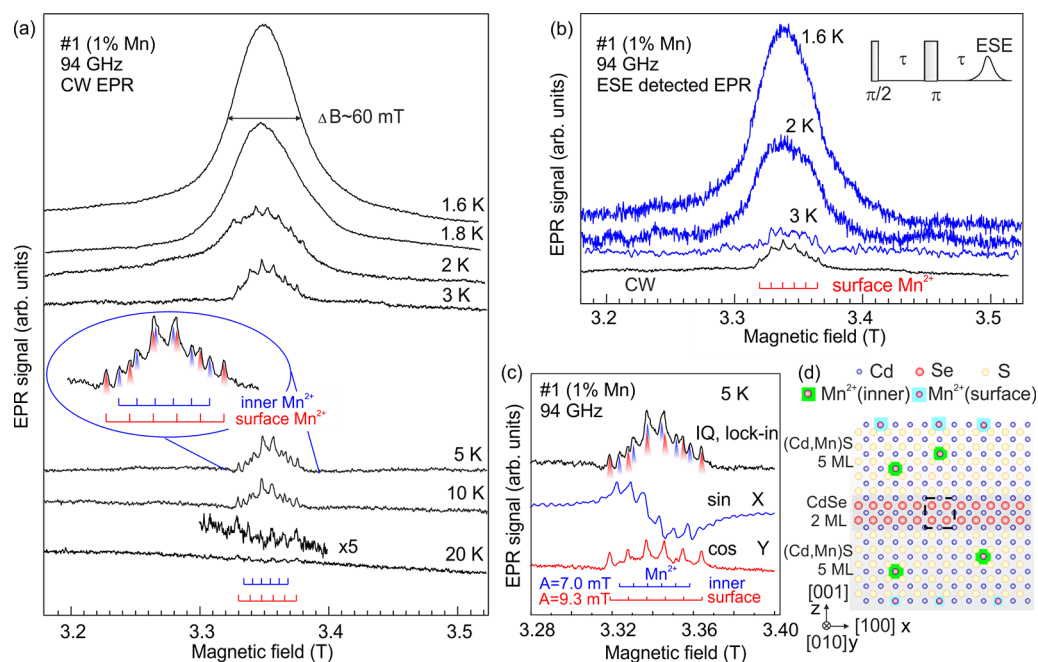


Figure 1. (a) CW EPR spectra recorded in CdSe/(Cd,Mn)S NPLs sample #1 in the temperature range of 1.6–20 K. (b) ESE-detected EPR spectra measured in the same sample at 1.6–3 K. For comparison, the CW EPR spectrum at 3 K is shown by the black line. (c) CW EPR spectra at 5 K from two outputs of the IQ detector, which allow us for distinguishing between inner and surface Mn. (d) Cartoon of a CdSe/(Cd,Mn)S NPL with 2/5 monolayers. The NPL has a cubic crystal lattice with the [001] axis for both CdSe and (Cd,Mn)S directed perpendicular to the NPL plane. A unit cell of a cubic crystal is marked with the thick dashed line.

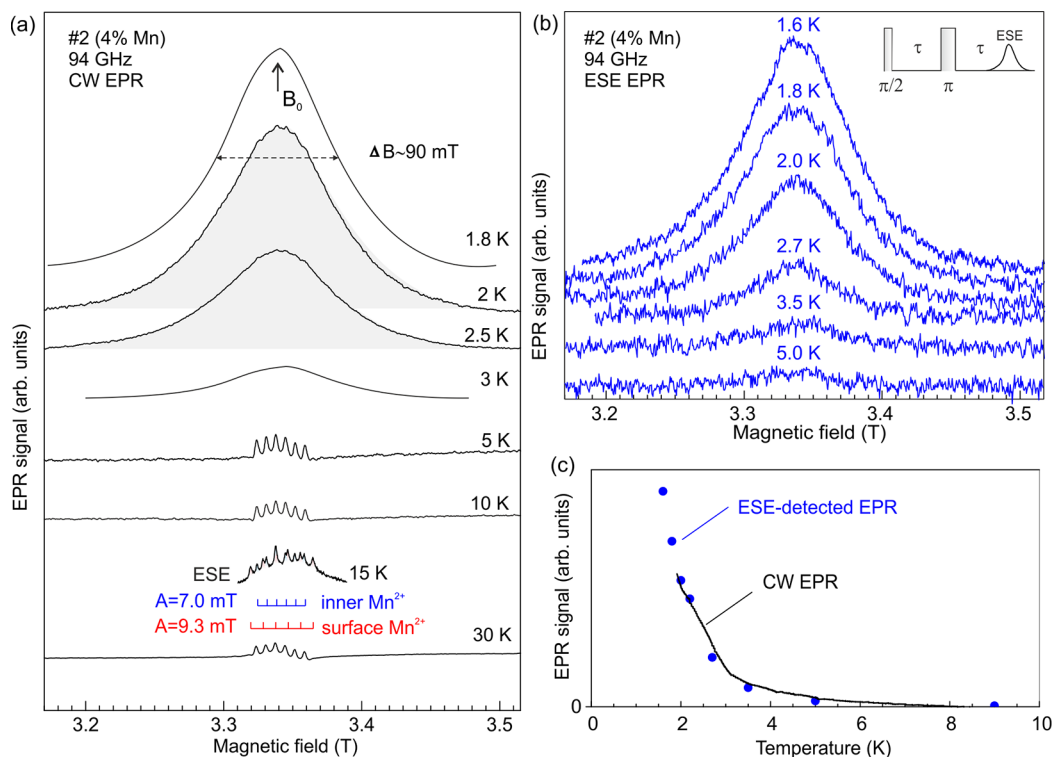


Figure 2. (a) CW EPR spectra recorded in CdSe/(Cd,Zn,Mn)S NPLs sample #2 in the temperature range of 1.8–30 K. The spectrum measured at $T = 15$ K via the electron spin echo and marked as ESE demonstrates that there are two types of Mn^{2+} centers in these NPLs, which differ in their detection conditions. (b) ESE-detected EPR spectra measured in the same sample at 1.6–5 K. (c) The temperature dependence of the CW EPR signal at magnetic field $B_0 = 3.3384$ T measured by scanning the temperature (black line) and of ESE-detected EPR signals (circles) measured at several fixed temperatures.

Figure 2a shows CW EPR spectra of the CdSe/(Cd,Zn,Mn)S NPLs sample #2 in a temperature range of 1.8–30 K. They are

similar to the spectra of sample #1. The intensity of the resolved Mn^{2+} spectra decreases at lower temperatures, and an intense

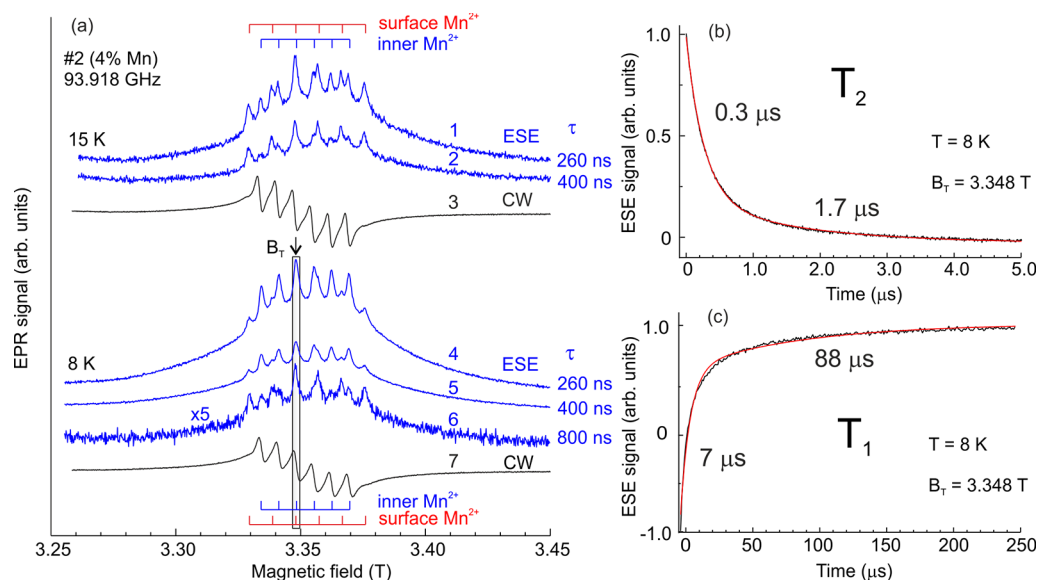


Figure 3. (a) EPR spectra of sample #2 measured at 8 and 15 K on a Bruker spectrometer in CW (spectra 3 and 7) and pulsed mode. The ESE-detected EPR (spectra 1, 2, 4–6) were measured using $\pi/2 - \tau - \pi$ pulse sequences with the $\pi/2$ pulse duration of 16 ns and $\tau = 260$ ns (1 and 4), 400 ns (2 and 5), and 800 ns (6). Experimental ESE decay (or recovery) curves to measure the spin–spin relaxation time T_2 (b) and spin–lattice relaxation time T_1 (c) at $T = 8$ K. Biexponential fits are shown by the red lines, the measurements are taken in a magnetic field $B_T = 3.348$ T as marked in (a) by the arrow.

broad line with width of 90 mT is measured at temperatures of 1.6–3 K. Also the ESE spectrum detected from the electron spin echo at $T = 15$ K is shown to demonstrate that both the inner and surface Mn^{2+} centers are present in the sample #2.

Figure 2b displays ESE-detected EPR spectra measured in the sample #2 at 1.6–5 K using the same pulse sequence as in Figure 1b. The intense broad line is similar to that observed in Figure 2a in CW EPR spectra, its intensity strongly decreases with increasing temperature. Figure 2c shows the temperature dependence of the EPR signal at a fixed value of the magnetic field $B_0 = 3.3384$ T, corresponding to the EPR maximum and measured by scanning the temperature for CW EPR (black line) and for ESE-detected EPR (blue circles). The EPR signal decays about exponentially with temperature.

Spin–Lattice and Spin–Spin Relaxation Times. To measure the spin dynamics of the Mn^{2+} ions, we used pulsed EPR in the electron spin echo regime. Figure 3a shows the EPR spectra of sample #2 measured at $T = 8$ and 15 K on a W-band Bruker spectrometer in pulsed (spectra 1, 2, and 4–6) and CW (spectra 3 and 7) mode. The ESE-detected EPR spectra were taken with the $\pi/2$ pulse duration of 16 ns, but with increasing interval τ between the $\pi/2$ and π pulses: $\tau = 260$ ns (spectra 1 and 4), 400 ns (spectra 2 and 5), and 800 ns (spectrum 6). All spectra contain EPR signals of the two types of individual manganese ions, characterized by the resolved structure with different hyperfine splitting constants $A = 7.0$ mT and 9.3 mT. The hyperfine structure sextet with $A = 7.0$ mT, which originates from inner Mn, dominates in the CW-EPR spectra. The ESE-detected EPR spectra also display a sextet with $A = 9.3$ mT, which arises from the surface Mn. The intensity of the signal from surface Mn is almost independent of the time interval τ between the $\pi/2$ and π pulses, while the relative intensity of the inner Mn is higher for shorter τ (compare 1 with 2, and 4 with 5 and 6). This evidences that the spin–spin relaxation time T_2 is shorter for the inner Mn than for the surface Mn. This behavior is expected for T_2 , as well as for T_1 , since inner Mn has more neighboring Mn atoms.

We measured the spin–lattice (T_1) and spin–spin (T_2) relaxation times of the Mn^{2+} ions in NPLs using ESE at 94 GHz. The measurements were carried out at $T = 8$ K in a magnetic field $B_T = 3.348$ T marked in Figure 3a by an arrow. In this field, the EPR lines for inner and surface Mn practically coincide. They correspond to the electronic transition $M_S = -1/2 \rightarrow M_S = +1/2$, and the same projection of the nuclear spin onto the magnetic field. The T_2 measurements were done using a $\pi/2 - \tau - \pi$ sequence with the $\pi/2$ pulse duration of 16 ns and τ varying from 200 ns to 10 μs . A part of the ESE decay curve is shown in Figure 3b by the black line. To measure T_1 , the ESE signal intensity was monitored by applying the inversion recovery pulse sequence $\pi - \Delta T - \pi/2 - \tau - \pi$, where ΔT was varied from 900 ns to 250 μs , while τ was kept at 200 ns. The result of these measurements is shown in Figure 3c by the black line. We fit these data with biexponential functions: $|y| = y_0 + C_F \exp(-t/t_F) + C_S \exp(-t/t_S)$, where t_F and t_S are characteristic relaxation times, “fast” and “slow”, and C_F and C_S are the weights of the two processes. The times T_1 and T_2 and the normalized contributions are given in Table 2. As discussed above, we

Table 2. Spin Relaxation Times of Mn Ions in Sample #2

Parameter		Value (μs)	Weight
Spin–lattice relaxation time	$T_{1,F}$	7	0.75
	$T_{1,S}$	88	0.25
Spin–spin relaxation time	$T_{2,F}$	0.3	0.80
	$T_{2,S}$	1.7	0.20

observe EPR signal from both inner and surface Mn. Since one type of Mn would have a single-exponential ESE signal, it is natural to assume that the “fast” and “slow” relaxation times correspond to inner and surface Mn. The larger weight for the inner Mn centers agrees with their larger EPR signals (see Figure 3a).

Obviously, the inner and surface Mn ions have a different environment. Most importantly, the surface Mn has about twice

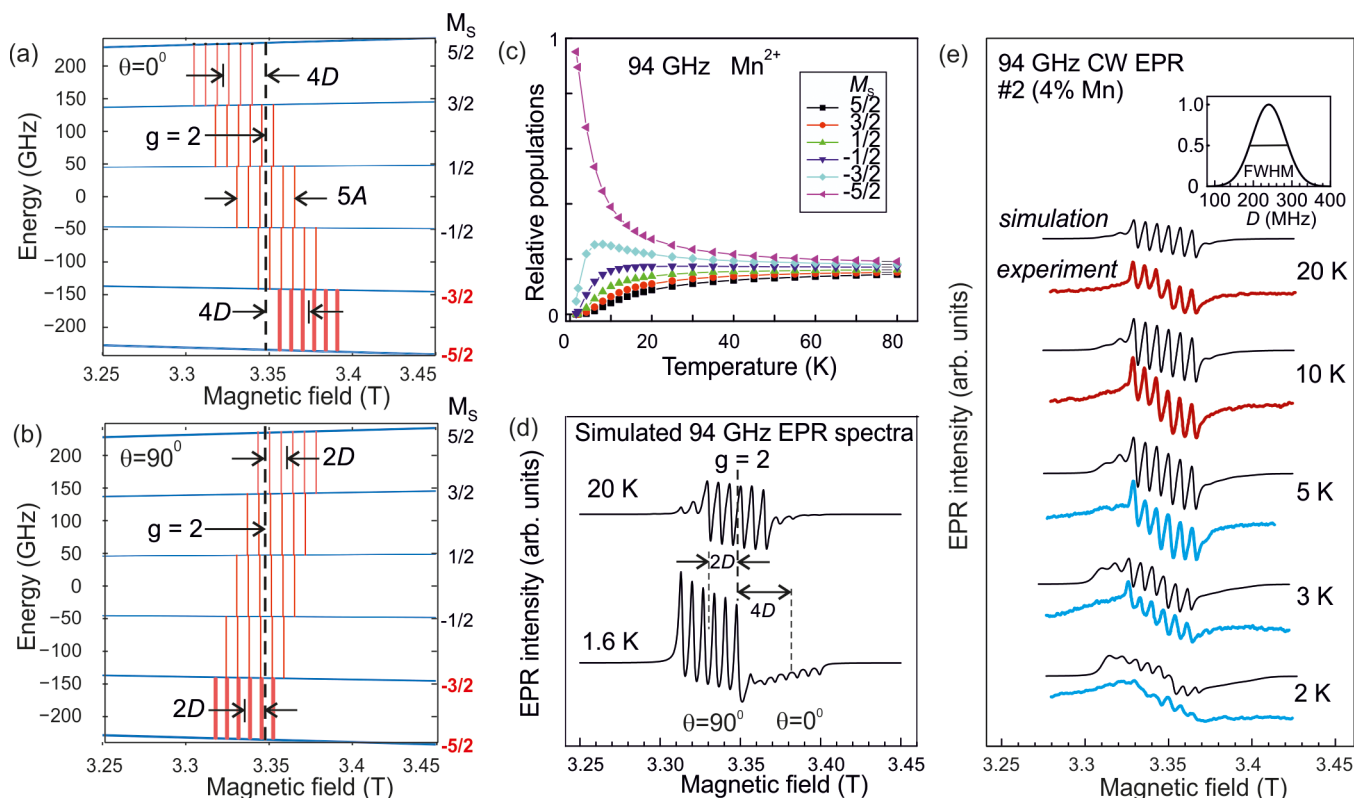


Figure 4. Energy levels of the Mn^{2+} ion ($S = 5/2$, $I = 5/2$) for a magnetic field oriented parallel (a) and perpendicular (b) to the NPL [001] axis. (c) Calculated relative populations of the six fine-structure levels of Mn^{2+} ions at the magnetic field corresponding to EPR at 94 GHz. The sum of the relative populations is 1 for any temperature. (d) Simulated EPR spectra at 94 GHz for a powder sample containing axial Mn^{2+} ions, $A = 7$ mT, $D = 9$ mT. (e) Comparison of the experimental CW EPR spectra measured in sample #2 at 94 GHz for different temperatures, and simulated EPR spectra of axial Mn^{2+} centers with the parameters given in the text. When recording these spectra, the phase of the IQ detector was adjusted to obtain EPR signals in the form of a derivative of the absorption line. The inset shows the Gaussian distribution of the D value used to simulate the spectra.

less neighboring Mn atoms than the inner Mn. It is known that both the spin–lattice (T_1) and spin–spin (T_2) relaxation times of the Mn^{2+} ions in II–VI semiconductors depend strongly on the Mn concentration.^{33,34} In fact, since the colloidal synthesis fails in an accurate control of the doping density, a postgrowth evaluation is required, and T_1 measurements provide a quite accurate estimation of the Mn concentration. $T_1 = 7$ and $88 \mu\text{s}$ correspond to about 4% and 2% Mn concentration, accordingly (see Figure 3e in ref 27). The second number is twice smaller and can be understood assuming that the surface Mn ions have less neighbors. The measured spin–spin relaxation times T_2 are much smaller than T_1 , which is typical for DMS. Our T_1 values are close to the ones reported in ODMR measurements,²⁷ and T_1 and T_2 are close to the relaxation times measured by a pulsed high-frequency EPR technique in Mn-doped ZnSe quantum dots.²⁶

Modeling of High-Frequency EPR Spectra of Mn^{2+} in an Axial Crystal Field. The studied NPLs are several monolayers thick and have lateral dimensions of tens of nm, therefore, they can be considered as two-dimensional systems similar to quantum wells. Changes in the crystal field caused by deformation in such systems lead to the splitting of the energy levels of paramagnetic ions with spin $S > 1/2$ in zero magnetic field and the appearance of a fine structure in the EPR spectra. This effect was observed in EPR studies of Mn^{2+} ions in semiconductor superlattices of ZnTe/MnTe and CdTe/MnTe grown by molecular-beam epitaxy.^{35,36} It is natural to assume

that in NPLs there is an axial crystal field normal to the NPL plane.

The EPR spectra of individual Mn^{2+} ions are described by the spin Hamiltonian:

$$H = g\mu_B \mathbf{B} \cdot \mathbf{S} + \mathbf{S} \cdot \mathbf{D} \cdot \mathbf{S} + \mathbf{A} \mathbf{I} \cdot \mathbf{S} \quad (1)$$

where μ_B is the Bohr magneton, $S = 5/2$, and $I = 5/2$. The first term describes the Zeeman interaction of electrons in a magnetic field; the g -factor of Mn^{2+} ions is practically isotropic and is close to the free electron g -factor of 2.0023. The second term describes the fine structure including the interaction of the electron spin with the crystal field, if it is present in NPLs. \mathbf{D} is the fine structure tensor characterizing this interaction. The last term describes the hyperfine interaction, that is, the interaction of the magnetic moment of the manganese electron shell with the magnetic moment of the nucleus ($I = 5/2$). The hyperfine interaction constant A is isotropic.

As discussed above, the inner Mn in samples #1 and #2 has a hyperfine structure constant close to that of bulk material, since the Mn^{2+} ion has a strongly localized electron shell. The fine structure splitting contains information on the crystal field. In bulk cubic (Cd,Mn)S, it is extremely small. The studied NPLs have a cubic crystal lattice, with the [001] axis directed perpendicular to the NPL plane. We assume that the in-plane crystal field is negligibly small, and the axial crystal field along the [001] direction equals $D[S_z^2 - (1/3)S(S+1)]$.

We calculated the energy levels and EPR transitions for axial Mn^{2+} centers ($S = 5/2$, $I = 5/2$) in a wide range of magnetic fields

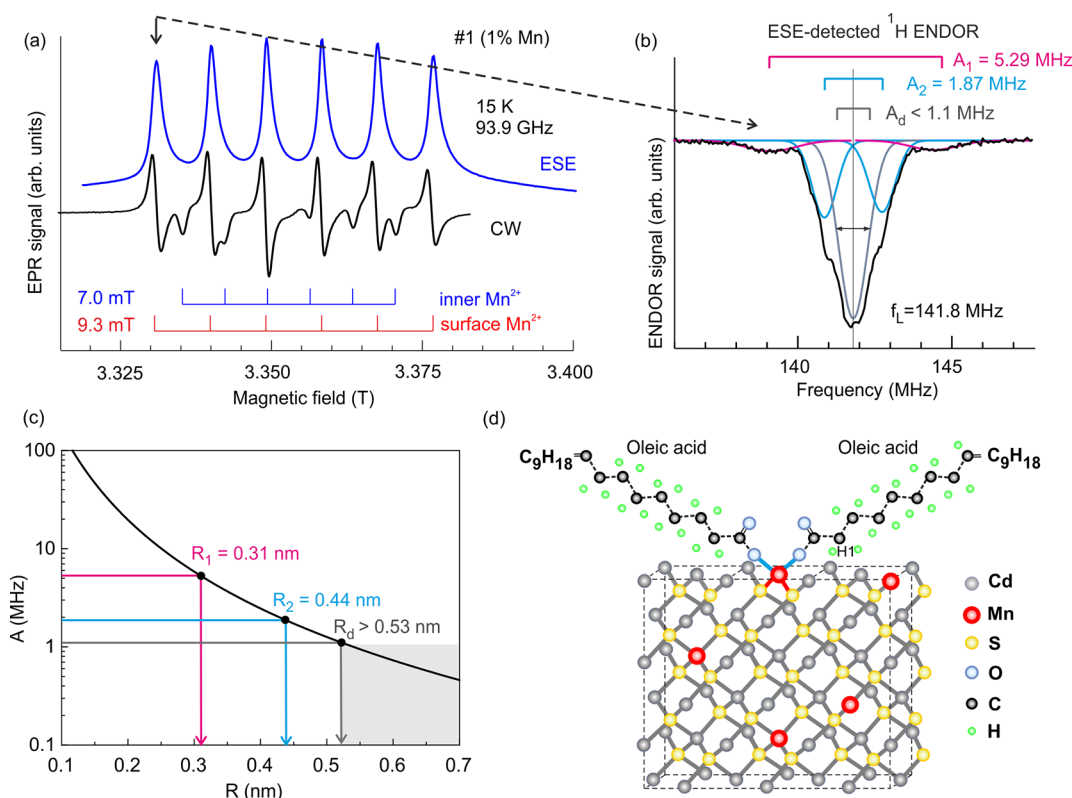


Figure 5. (a) EPR spectra recorded at 93.9 GHz and $T = 15$ K on sample #1: (top) ESE-detected EPR and (bottom) CW EPR. (b) ESE-detected ENDOR spectrum measured in a magnetic field corresponding to the EPR of the surface Mn^{2+} ions, f_L is the Larmor frequency of the ^1H nucleus in a magnetic field marked with the arrow in (a). (c) Dependence of the hydrogen hyperfine interaction constant A_i on the distance R between the Mn^{2+} electron spin and the i -th ^1H nucleus. Circles mark the A_i values determined from the ENDOR spectrum. (d) Mn^{2+} -doped CdS shell of the NPL and oleic acid ligands, which passivate the surface Mn^{2+} ion. The hydrogen atom marked as H1 is located at the distance R_1 from a Mn^{2+} ion.

using the software packages developed by Grachev³⁷ and EasySpin.³⁸ We used the following parameters: $g = 2.003$, $A = 7$ mT (195 MHz), and $D = 9$ mT (240 MHz); the details are explained in the Supporting Information S2. Figure 4a,b shows the calculated energy levels of the axial Mn^{2+} center and the 94 GHz EPR transitions for a magnetic field oriented parallel ($\theta = 0^\circ$) and perpendicular ($\theta = 90^\circ$) to the NPL [001] axis. The dashed lines mark the magnetic field corresponding to $g = 2$.

At thermal equilibrium, the populations of the levels are determined by the Boltzmann distribution. Figure 4c displays the temperature dependence of the populations of the levels $M_S = -5/2, -3/2, -1/2, +1/2, +3/2, +5/2$ normalized so that the sum of the populations of all six levels equals 1. At $T = 1.6$ K, the lowest Mn^{2+} level is predominantly populated, and the EPR transition $-5/2 \leftrightarrow -3/2$ is the most intense. In Figure 4a,b, the intensity of the EPR transitions (vertical red lines) is according to the convention shown by the line thickness.

It is reasonable to assume that the NPLs are randomly oriented due to the way of sample preparation (Methods). Therefore, their EPR spectra can be calculated by simulating the EPR spectra of powdered samples. In such calculations, the spectra for all NPL orientations relative to the magnetic field are averaged. Figure 4d shows simulated EPR spectra at two temperatures, we assumed that each EPR line has a line width $\Delta B = 2$ mT. The number of NPLs with an orientation close to perpendicular is much larger than the number of NPLs with the axis oriented about parallel to the field. Therefore, in the EPR spectra recorded at $T = 1.6$ K, the hyperfine structure bundle, corresponding to the electronic transition $M_S = -5/2 \leftrightarrow M_S =$

$-3/2$ for perpendicularly oriented NPL axes, is the most intense (Figure 4d, bottom). This bundle is shifted relative to $g = 2$ to lower fields by $2D$ (compare with Figure 4b). The bundle corresponding to $\theta = 0^\circ$ has much lower intensity and is shifted to higher fields by $4D$ (compare with Figure 4a). At the elevated temperature of 20 K, EPR lines corresponding to all transitions appear and the EPR spectrum becomes symmetrical (Figure 4d, top). As a result, the EPR spectra recorded at low and high temperatures differ significantly.

In real systems there is a certain spread of stress, resulting in the associated spread of the fine structure splitting parameter D . We take this spread into account for modeling the experimental EPR spectra. Figure 4e (black lines) shows the simulated EPR spectra of Mn^{2+} calculated for the following parameters of the spin Hamiltonian: $g = 2.003$, $A = 7.0$ mT (195 MHz), $D = 9$ mT (240 MHz), and a Gaussian distribution of D with a full-width at half-maximum (fwhm) of 100 MHz, which is shown in the inset of Figure 4e. The individual EPR line width ΔB is 2 mT. In this simulation, we did not take into account the EPR of surface Mn since in the CW EPR spectra of sample #2 these signals are weak. The results of the calculations are compared with the measured CW EPR spectra of the sample #2 (Figure 4e, colored lines) and demonstrate satisfactory agreement with experiment. We would like to stress that the EPR spectra from such a complex and inhomogeneous system as randomly oriented NPL ensembles can be described using a simple model with only one fitting parameter D . The other parameters, the g -factor and A , are determined experimentally with high accuracy.

ENDOR Measurements. The surface Cd^{2+} ions, which terminate the NPLs on both sides, have two dangling molecular bonds linked to CH groups via oxygen belonging to the oleic acid. Since Mn substitutes for Cd, it is reasonable to assume that the same is true for surface Mn^{2+} ions, which also possess two dangling bonds linked to CH groups via oxygen of the oleic acid (Figure 5d). As a result, there is a dipole–dipole interaction between the magnetic moments of the electron shell of Mn^{2+} ions and the magnetic moments of hydrogen nuclei. We used a high-frequency ENDOR technique to detect this interaction. Note that Mn^{2+} can also interact with the carbon isotope ^{13}C , which has a nuclear magnetic moment, but the concentration of this isotope is extremely low (1.1%) and it is difficult to detect such interaction.

Figure 5a shows EPR spectra recorded at 93.9 GHz and $T = 15$ K on sample #1: ESE-detected EPR (top) and CW EPR (bottom). The spectra are dominated by the contribution of Mn^{2+} ions located on the NPLs surface. To measure ENDOR, the magnetic field is set to the EPR line (we selected the low-field EPR line of the surface Mn sextet, as shown in Figure 5a by the arrow), and a sequence of three microwave pulses is applied: $\pi/2 - \tau_1 - \pi/2 - \tau_2 - \pi/2$ (so-called Mims sequence). Here, the three pulses have durations of $\pi/2$ and are delayed by times τ_1 and τ_2 . The second pause τ_2 is long, and during this time, the radiofrequency (RF) pulse is applied, and after that the ESE signal is detected. The RF scans a certain range, and when it matches the resonance frequency of one of the surrounding nuclei, the ESE signal is reduced and the ENDOR signal is detected.

Figure 5b presents the ESE-detected ENDOR as a function of the RF pulse frequency. Here f_L is the Larmor frequency of the ^1H nucleus, $f_L = (1/h)g\mu_N B$, g is the g -factor of the ^1H nucleus, μ_N is the nuclear magneton. $\pi/2 = 150$ ns, $\tau_1 = 400$ ns, and the typical pulse length of the RF pulse is 0.1 ms. The line consists of several contours located symmetrically about the center. Each contour corresponds to an ENDOR transition with the following frequency:

$$f_{\text{ENDOR}_i} = f_L \pm A_i/2 \quad (2)$$

where A_i is the hyperfine interaction constant with the i -th hydrogen nucleus, that is, each ^1H nucleus gives rise to two ENDOR transitions symmetrically placed around the ^1H nuclear Larmor frequency f_L . The result of the decomposition of the ENDOR signal into Gaussian lines is presented in Figure 5b by thin lines. The fitting reveals three hyperfine interaction constants: $A_1 = 5.29$ MHz, $A_2 = 1.87$ MHz, and $A_d < 1.1$ MHz. Each of these values corresponds to a certain distance R_i to the i -th nucleus, that is, the signals marked as A_1 and A_2 originate from the nearby ^1H nuclei, and the broad line centered at the Larmor frequency is due to numerous distant ^1H nuclei.

Two magnetic moments, electron and i -th ^1H nucleus, located at a distance R_i are coupled by dipole–dipole interaction resulting in an axial, traceless hyperfine tensor oriented along their connection line with a principal value $A_i = (\mu_0/4\pi h) g_e \mu_B g_i \mu_N (2/R_i^3)$, where g_e and g_i are the electron and nuclear g -factors, respectively, μ_B is the Bohr magneton, and μ_0 is vacuum permeability. This dependence is plotted in Figure 5c (line), where the circles correspond to the A_1 , A_2 , and A_d values. From this we conclude that the manganese ion at the NPL surface interacts with hydrogen nuclei located at distances $R_1 = 0.31 \pm 0.04$ nm, $R_2 = 0.44 \pm 0.09$ nm, and distant nuclei displaced by $R_d > 0.53$ nm.

Figure 5d shows the five monolayer-thick CdS shell of the NPL doped with Mn^{2+} ions. Oleic acid ligands, which passivate the surface Mn, are conventionally drawn, and the oxygen and hydrogen atoms in the ligand chain are shown. The hydrogen atom located at distance R_1 from the Mn^{2+} ion is marked as H1.

The distances R_1 and R_2 between the surface Mn and the two nearest ^1H nuclei are reasonable, considering the covalent bond length of Mn–O (about 0.22 nm), O–C (about 0.14 nm), C–C (about 0.15 nm), and C–H (about 0.11 nm) as well as the bond angles between these atoms. We cannot distinguish whether these two nearest nuclei belong to the same ligand or not. Well-defined peaks corresponding to R_1 evidence that all ligands are attached to surface Mn in the same manner, forming an ordered structure. This suggests that the ENDOR technique can be extended to study ligand attachment to NPL surface.

We also measured 35 GHz ODMR on sample #2. The obtained ODMR spectra reproduce previously reported ODMR in similar NPLs.^{27–29} The comparison of these spectra with ODMR in Mn-doped yttrium aluminum garnet crystals³⁹ allows us to suppose that the ODMR spectra of NPLs belong to complexes of interacting Mn^{2+} ions. Details are given in the Supporting Information S4.

CONCLUSIONS

By using high-frequency EPR spectroscopy of magnetic Mn^{2+} ions implemented in semiconductor CdSe/(Cd,Mn)S nanoplatelets, we have obtained detailed information on their location, spin dynamics, and interaction of the surface Mn^{2+} ions with the ^1H nuclei belonging to oleic acid ligands that passivate the NPL surface. This study proves that magnetic resonance techniques are a powerful tool to study colloidal nanocrystals. A challenging development here would be experimental detection of the surface spins of dangling bonds in diamagnetic nanocrystals, which have been recently detected in magneto-optical experiments, by these techniques.^{7,9}

METHODS

The NPLs samples were prepared using a modified procedure of the c-ALD recipe as described in the Supporting Information S1.

For the EPR measurements, a dispersion of NPLs was precipitated inside a quartz test tube with a diameter of about 3 mm and a height of 5 mm and dried. The procedure was repeated 3 times to increase the number of NPLs. Thus, the samples contained NPLs at the walls and at the bottom of the tube. For measurements on the W-band Bruker spectrometer, the dispersion of NPLs was inserted in quartz test tubes with an inner diameter of approximately 0.9 mm and was frozen. Therefore, we can assume that in both cases, the NPLs in the ensembles had completely random orientation and their EPR spectra behave similar to powder samples.

EPR spectra were recorded at a frequency of 94 GHz using the high-frequency EPR-ODMR spectrometer developed at the Ioffe Institute in cooperation with the DOK company.⁴⁰ It allows measurements of EPR in CW and pulsed (free induction decay, FID and ESE) mode, photo-EPR and ODMR in a wide range of temperatures (1.6 to 300 K) and magnetic fields (up to 7 T with the ability to invert the field direction). The microwave bridge of this spectrometer has a powerful microwave generator, a superheterodyne receiver, and an inphase-quadrature (IQ) detector. Some ESE-detected EPR and ENDOR measurements were carried out with a Bruker E680 spectrometer. The EPR spectra in pulsed mode were recorded by monitoring the ESE signal following a microwave $\pi/2$ - and a π -pulse sequence as a function of magnetic field. The ENDOR spectra were obtained by monitoring the intensity of the stimulated echo, following three microwave $\pi/2$ -pulses, as a function of the frequency of a radio frequency pulse applied between the second and the third microwave pulses (Mims-type of stimulated-echo pulse

sequence). ODMR at the frequency of 35 GHz was recorded by monitoring the intensity of the photoluminescence excited with a semiconductor laser.

ASSOCIATED CONTENT

Supporting Information

The Supporting Information is available free of charge at <https://pubs.acs.org/doi/10.1021/acsnano.2c10123>.

Sample preparation details; calculated energy level diagram of manganese ions in a magnetic field; discussion of the covalence effects; ODMR spectra (PDF)

AUTHOR INFORMATION

Corresponding Authors

Roman A. Babunts – Ioffe Institute, Russian Academy of Sciences, 194021 St. Petersburg, Russia;
Email: roman.babunts@mail.ioffe.ru

Elena V. Shornikova – Experimentelle Physik 2, Technische Universität Dortmund, 44227 Dortmund, Germany;
orcid.org/0000-0002-6866-9013;
Email: elena.shornikova@tu-dortmund.de

Dmitri R. Yakovlev – Ioffe Institute, Russian Academy of Sciences, 194021 St. Petersburg, Russia; Experimentelle Physik 2, Technische Universität Dortmund, 44227 Dortmund, Germany; orcid.org/0000-0001-7349-2745;
Email: dmitri.yakovlev@tu-dortmund.de

Authors

Yulia A. Uspenskaya – Ioffe Institute, Russian Academy of Sciences, 194021 St. Petersburg, Russia

Nikolai G. Romanov – Ioffe Institute, Russian Academy of Sciences, 194021 St. Petersburg, Russia; orcid.org/0000-0002-5330-2569

Sergei B. Orlinskii – Kazan Federal University, Institute of Physics, 420008 Kazan, Russia

Georgiy V. Mamin – Kazan Federal University, Institute of Physics, 420008 Kazan, Russia; orcid.org/0000-0002-7852-917X

Manfred Bayer – Experimentelle Physik 2, Technische Universität Dortmund, 44227 Dortmund, Germany;
orcid.org/0000-0002-0893-5949

Furkan Isik – Department of Electrical and Electronics Engineering, Department of Physics, UNAM – Institute of Materials Science and Nanotechnology, Bilkent University, 06800 Ankara, Turkey; orcid.org/0000-0001-5881-5438

Sushant Shendre – Luminous! Center of Excellence for Semiconductor Lighting and Displays, School of Electrical and Electronic Engineering, Division of Physics and Applied Physics, School of Physical and Mathematical Sciences, School of Materials Science and Engineering, Nanyang Technological University, 639798, Singapore; orcid.org/0000-0001-8586-7145

Savas Delikanli – Luminous! Center of Excellence for Semiconductor Lighting and Displays, School of Electrical and Electronic Engineering, Division of Physics and Applied Physics, School of Physical and Mathematical Sciences, School of Materials Science and Engineering, Nanyang Technological University, 639798, Singapore; Department of Electrical and Electronics Engineering, Department of Physics, UNAM – Institute of Materials Science and Nanotechnology, Bilkent University, 06800 Ankara, Turkey; orcid.org/0000-0002-0613-8014

Hilmi Volkan Demir – Luminous! Center of Excellence for Semiconductor Lighting and Displays, School of Electrical and Electronic Engineering, Division of Physics and Applied Physics, School of Physical and Mathematical Sciences, School of Materials Science and Engineering, Nanyang Technological University, 639798, Singapore; Department of Electrical and Electronics Engineering, Department of Physics, UNAM – Institute of Materials Science and Nanotechnology, Bilkent University, 06800 Ankara, Turkey; orcid.org/0000-0003-1793-112X

Pavel G. Baranov – Ioffe Institute, Russian Academy of Sciences, 194021 St. Petersburg, Russia

Complete contact information is available at:

<https://pubs.acs.org/doi/10.1021/acsnano.2c10123>

Notes

The authors declare no competing financial interest.

ACKNOWLEDGMENTS

The authors acknowledge the support of the Russian Foundation for Basic Research under grant no. 19-52-12058. E.V.S. acknowledges DFG grant no.: 462009643. D.R.Y. acknowledges DFG support through the International Collaborative Research Center TRR 160 (Project C7, B1). H.V.D., S.S., F.L., and S.D. gratefully acknowledge the financial support in part from the Singapore Agency for Science, Technology and Research (A*STAR) SERC Pharos Program under grant number 152-73-00025 and Agency for Science, Technology and Research (A*STAR) MTC program under grant number M21J9B0085, Ministry of Education Tier 1 under grant number MOE-RG62/20 (Singapore) and in part from TUBITAK 119N343, 121C266, 121N395 and 20AG001. H.V.D. also acknowledges support from TUBA and TUBITAK 2247-A National Leader Researchers Program (121C266).

REFERENCES

- (1) Ithurria, S.; Dubertret, B. Quasi 2D Colloidal CdSe Platelets with Thicknesses Controlled at the Atomic Level. *J. Am. Chem. Soc.* **2008**, *130*, 16504–16505.
- (2) Li, Z.; Peng, X. Size/Shape-Controlled Synthesis of Colloidal CdSe Quantum Disks: Ligand and Temperature Effects. *J. Am. Chem. Soc.* **2011**, *133*, 6578–6586.
- (3) Tessier, M. D.; Javaux, C.; Maksimovic, I.; Lorient, V.; Dubertret, B. Spectroscopy of Single CdSe Nanoplatelets. *ACS Nano* **2012**, *6*, 6751–6758.
- (4) Delikanli, S.; Guzelurk, B.; Hernández-Martínez, P. L.; Erdem, T.; Kelestemur, Y.; Olutas, M.; Akgul, M. Z.; Demir, H. V. Continuously Tunable Emission in Inverted Type-I CdS/CdSe Core/Crown Semiconductor Nanoplatelets. *Adv. Funct. Mater.* **2015**, *25*, 4282–4289.
- (5) Antanovich, A. V.; Prudnikau, A. V.; Melnikau, D.; Rakovich, Y. P.; Chuvilin, A.; Woggon, U.; Achtstein, A. W.; Artemyev, M. V. Colloidal Synthesis and Optical Properties of Type-II CdSe-CdTe and Inverted CdTe-CdSe Core-Wing Heteronanoplatelets. *Nanoscale* **2015**, *7*, 8084–8092.
- (6) Delikanli, S.; Yu, G.; Yeltik, A.; Bose, S.; Erdem, T.; Yu, J.; Erdem, O.; Sharma, M.; Sharma, V. K.; Quliyeva, U.; Shendre, S.; Dang, C.; Zhang, D. H.; Sum, T. C.; Fan, W.; Demir, H. V. Ultrathin Highly Luminescent Two-Monolayer Colloidal CdSe Nanoplatelets. *Adv. Funct. Mater.* **2019**, *29*, 1901028.
- (7) Rodina, A.; Efros, A. L. Magnetic Properties of Nonmagnetic Nanostructures: Dangling Bond Magnetic Polaron in CdSe Nanocrystals. *Nano Lett.* **2015**, *15*, 4214–4222.
- (8) Biadala, L.; Shornikova, E. V.; Rodina, A. V.; Yakovlev, D. R.; Siebers, B.; Aubert, T.; Nasilowski, M.; Hens, Z.; Dubertret, B.; Efros,

- Al. L.; Bayer, M. Magnetic Polarons on Dangling-Bond Spins in CdSe Colloidal Nanocrystals. *Nat. Nanotechnol.* **2017**, *12*, 569–574.
- (9) Shornikova, E. V.; Golovatenko, A. A.; Yakovlev, D. R.; Rodina, A. V.; Biadala, L.; Qiang, G.; Kuntzmann, A.; Nasilowski, M.; Dubertret, B.; Polovitsyn, A.; Moreels, I.; Bayer, M. Surface Spin Magnetism Controls the Polarized Exciton Emission from CdSe Nanoplatelets. *Nat. Nanotechnol.* **2020**, *15*, 277–282.
- (10) Ithurria, S.; Talapin, D. V. Colloidal Atomic Layer Deposition (c-Ald) Using Self-Limiting Reactions at Nanocrystal Surface Coupled to Phase Transfer Between Polar and Nonpolar Media. *J. Am. Chem. Soc.* **2012**, *134*, 18585–18590.
- (11) Mahler, B.; Nadal, B.; Bouet, C.; Patriarche, G.; Dubertret, B. Core/Shell Colloidal Semiconductor Nanoplatelets. *J. Am. Chem. Soc.* **2012**, *134*, 18591–18598.
- (12) Furdyna, J. K. Diluted Magnetic Semiconductors. *J. Appl. Phys.* **1988**, *64*, R29–R64.
- (13) Bussian, D. A.; Crooker, S. A.; Yin, M.; Brynda, M.; Efros, A. L.; Klimov, V. I. Tunable Magnetic Exchange Interactions in Manganese Doped Inverted Core-Shell ZnSe-CdSe Nanocrystals. *Nat. Mater.* **2009**, *8*, 35–40.
- (14) Furdyna, J. K.; Lee, S.; Dobrowolska, M.; Wojtowicz, T.; Liu, X. Band-Offset Engineering in Magnetic/Non-Magnetic Semiconductor Quantum Structures. In *Introduction to the Physics of Diluted Magnetic Semiconductors*; Kossut, J., Gaj, J. A., Eds.; Springer Verlag: Berlin, Heidelberg, 2010; pp 103–160.
- (15) Delikanli, S.; Akgul, M. Z.; Murphy, J. R.; Barman, B.; Tsai, Y.; Scrase, T.; Zhang, P.; Bozok, B.; Hernandez-Martinez, P. L.; Christodoulides, J.; Cartwright, A. N.; Petrou, A.; Demir, H. V. Mn²⁺-Doped CdSe/CdS Core/Multishell Colloidal Quantum Wells Enabling Tunable Carrier-Dopant Exchange Interactions. *ACS Nano* **2015**, *9*, 12473–12479.
- (16) Muckel, F.; Delikanli, S.; Hernandez-Martinez, P. L.; Priesner, T.; Lorenz, S.; Ackermann, J.; Sharma, M.; Demir, H. V.; Bacher, G. sp-d Exchange Interactions in Wave Function Engineered Colloidal CdSe/Mn:CdS Hetero-Nanoplatelets. *Nano Lett.* **2018**, *18*, 2047–2053.
- (17) Lorenz, S.; Bieniek, J.; Erickson, C. S.; Gamelin, D. R.; Fainblat, R.; Bacher, G. Orientation of Individual Anisotropic Nanocrystals Identified by Polarization Fingerprint. *ACS Nano* **2021**, *15*, 13579–13590.
- (18) Davis, A. H.; Hofman, E.; Chen, K.; Li, Z.-J.; Khammang, A.; Zamani, H.; Franck, J. M.; Maye, M. M.; Meulenberg, R. W.; Zheng, W. Exciton Energy Shifts and Tunable Dopant Emission in Manganese Doped Two-Dimensional CdS/ZnS Core/Shell Nanoplatelets. *Chem. Mater.* **2019**, *31*, 2516–2523.
- (19) Couston, G.; Esnouf, S.; Gacoin, T.; Boilot, J.-P. CdS:Mn Nanocrystals in Transparent Xerogel Matrices. *J. Phys. Chem.* **1996**, *100*, 20021–20026.
- (20) Zheng, W.; Wang, Z.; Wright, J.; Goundie, B.; Dalal, N. S.; Meulenberg, R. W.; Strouse, G. F. Probing the Local Site Environments in Mn:CdSe Quantum Dots. *J. Phys. Chem. C* **2011**, *115*, 23305–23314.
- (21) Nistor, S. V.; Stefan, M.; Nistor, L. C.; Kuncser, V.; Ghica, D.; Vlaicu, I. D. Aggregates of Mn²⁺ Ions in Mesoporous Self-Assembled Cubic ZnS:Mn Quantum Dots: Composition, Localization, Structure, and Magnetic Properties. *J. Phys. Chem. C* **2016**, *120*, 14454–14466.
- (22) Hofmann, D. M.; Hofstaetter, A.; Leib, U.; Meyer, B. K.; Couston, G. EPR and ENDOR Investigations on CdS:Mn Nanocrystals. *J. Cryst. Growth* **1998**, *184*–185, 383–387.
- (23) Ochsenbein, S. T.; Gamelin, D. R. Quantum Oscillations in Magnetically Doped Colloidal Nanocrystals. *Nat. Nanotechnol.* **2011**, *6*, 112–115.
- (24) Schimpf, A. M.; Ochsenbein, S. T.; Gamelin, D. R. Surface Contributions to Mn²⁺ Spin Dynamics in Colloidal Doped Quantum Dots. *Phys. Chem. Lett.* **2015**, *6*, 457–463.
- (25) Moro, F.; Turyanska, L.; Wilman, J.; Williams, H. E. L.; Fielding, A. J.; Patanè, A. Surface Sensing of Quantum Dots by Electron Spins. *Nano Lett.* **2016**, *16*, 6343–6348.
- (26) Bindra, J. K.; Singh, K.; van Tol, J.; Dalal, N. S.; Strouse, G. F. Spin Dynamics in Mn:ZnSe Quantum Dots: A Pulsed High-Frequency EPR Study. *J. Phys. Chem. C* **2020**, *124*, 19348–19354.
- (27) Shornikova, E. V.; Yakovlev, D. R.; Tolmachev, D. O.; Ivanov, V. Yu.; Kalitukha, I. V.; Sapega, V. F.; Kudlacik, D.; Kusrayev, Yu. G.; Golovatenko, A. A.; Shendre, S.; Delikanli, S.; Demir, H. V.; Bayer, M. Magneto-Optics of Excitons Interacting with Magnetic Ions in CdSe/CdMnS Colloidal Nanoplatelets. *ACS Nano* **2020**, *14*, 9032–9041.
- (28) Strassberg, R.; Delikanli, S.; Barak, Y.; Dehnel, J.; Kostadinov, A.; Maikov, G.; Hernandez-Martinez, P. L.; Sharma, M.; Demir, H. V.; Lifshitz, E. Persuasive Evidence for Electron-Nuclear Coupling in Diluted Magnetic Colloidal Nanoplatelets Using Optically Detected Magnetic Resonance Spectroscopy. *J. Phys. Chem. Lett.* **2019**, *10*, 4437–4447.
- (29) Tolmachev, D. O.; Ivanov, V. Yu.; Yakovlev, D. R.; Shornikova, E. V.; Witkowski, B.; Shendre, S.; Isik, F.; Delikani, S.; Demir, H. V.; Bayer, M. Optically Detected Magnetic Resonance in CdSe/CdMnS Nanoplatelets. *Nanoscale* **2020**, *12*, 21932–21939.
- (30) Shendre, S.; Delikanli, S.; Li, M.; Dede, D.; Pan, Z.; Ha, S. T.; Fu, Y. H.; Hernandez-Martinez, P. L.; Yu, J.; Erdem, O.; Kuznetsov, A. I.; Dang, C.; Sum, T. C.; Demir, H. V. Ultrahigh-Efficiency Aqueous Flat Nanocrystals of CdSe/CdS and Cd_{1-x}Zn_xS Colloidal Core/Crown and Alloyed-Shell Quantum Wells. *Nanoscale* **2019**, *11*, 301–310.
- (31) Dorain, P. B. Electron Paramagnetic Resonance of Manganese (II) in Hexagonal Zinc Oxide and Cadmium Sulfide Single Crystals. *Phys. Rev.* **1958**, *112*, 1058–1060.
- (32) Šimánek, E.; Müller, K. A. Covalency and Hyperfine Structure Constant *A* of Iron Group Impurities in Crystals. *J. Phys. Chem. Solids* **1970**, *31*, 1027–1040.
- (33) Yakovlev, D. R.; Ossau, W. Magnetic Polarons. In *Introduction to the Physics of Diluted Magnetic Semiconductors*; Kossut, J., Gaj, J. A., Eds.; Springer Series in Materials Science; Springer Verlag: Berlin, Heidelberg, 2010; pp 221–262.
- (34) Yakovlev, D. R.; Merkulov, I. A. Spin and energy transfer between carriers, magnetic ions, and lattice. In *Introduction to the Physics of Diluted Magnetic Semiconductors*; Kossut, J., Gaj, J. A., Eds.; Springer Series in Materials Science; Springer Verlag: Berlin, Heidelberg, 2010; pp 263–303.
- (35) Qazzaz, M.; Yang, G.; Xin, S. H.; Montes, L.; Luo, H.; Furdyna, J. K. Electron Paramagnetic Resonance of Mn²⁺ in Strained-Layer Semiconductor Superlattices. *Solid State Commun.* **1995**, *96*, 405–409.
- (36) Bogucki, A.; Goryca, M.; Łopion, A.; Pacuski, W.; Polczyńska, K. E.; Domagała, J. Z.; Tokarczyk, M.; Fąs, T.; Golnik, A.; Kossacki, P. Angle-Resolved Optically Detected Magnetic Resonance as a Tool for Strain Determination in Nanostructures. *Phys. Rev. B* **2022**, *105*, 075412.
- (37) Grachev, V. G. Correct Expression for the Generalized Spin Hamiltonian for a Noncubic Paramagnetic Center. *JETP* **1987**, *65*, 1029–1035.
- (38) Stoll, S.; Schweiger, A. EasySpin, a Comprehensive Software Package for Spectral Simulation and Analysis in EPR. *J. Magn. Reson.* **2006**, *178*, 42–55.
- (39) Edinach, E. V.; Kramushchenko, D. D.; Gurin, A. S.; Uspenskaya, Yu. A.; Babunts, R. A.; Asatryan, H. R.; Badalyan, A. G.; Romanov, N. G.; Baranov, P. G. Evidence of the Excitation of Mn²⁺ Spin-Dependent Photoluminescence in Manganese-Doped Yttrium Aluminum Garnets. *Appl. Magn. Reson.* **2019**, *50*, 1315–1324.
- (40) Babunts, R. A.; Badalyan, A. G.; Gurin, A. S.; Romanov, N. G.; Baranov, P. G.; Nalivkin, A. V.; Bogdanov, L. Yu.; Korneev, D. O. Capabilities of Compact High-Frequency EPR/ESE/ODMR Spectrometers Based on a Series of Microwave Bridges and a Cryogen-Free Magneto-Optical Cryostat. *Appl. Magn. Reson.* **2020**, *51*, 1125–1143.